CRYSTAL GROWTH & DESIGN

pubs.acs.org/crystal

Article

Mapping of Structural Changes Induced by X-ray Nanopatterning via Nano-X-ray Diffraction and Corresponding Electrical Effects

Muhammad Waqas Rabbani, Valentina Bonino, Luca Spessa, Angelo Agostino, Natascia De Leo, Carmelo Prestipino, and Marco Truccato*

Cite This: *Cryst. Growth Des.* 2021, 21, 3299–3309

Read Online

ACCESS | Metrics & More | Article Recommendations | Supporting Information

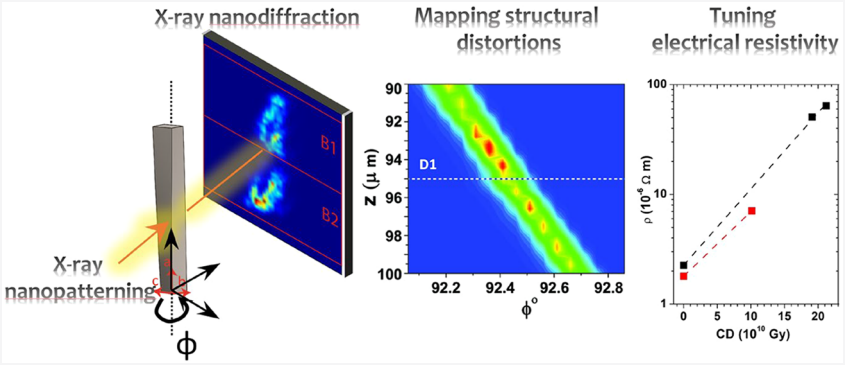

ABSTRACT: We have investigated the modifications induced in high-T_c superconductor $Bi_2Sr_2CaCu_2O_{8+\delta}$ (Bi-2212) single crystals by irradiation with an X-ray nanobeam 250 × 250 nm^2 in size with E = 14.85 keV and a time-averaged photon flux $\Phi_0 = 7.53 \times 10^8$ ph s^{-1}. Crystals were mounted onto amorphous substrates with electrical contacts to allow for both X-ray diffraction (XRD) and electrical measurements on the same sample. Changes in the domain structure were monitored via space-resolved nano-XRD mapping, whereas electrical properties were measured off-line at different levels of irradiation dose. The results show that irradiation induces both an increase of the mosaicity spread and a localized release of the mechanical stress of the crystals. This implies a transient local change of mechanical properties that could be due to thermal fatigue or nonthermal melting. Analysis of the electrical properties of the irradiated regions indicates a strong underdoping effect by the nanobeam and an exponential increase of the normal-state resistivity with the irradiation dose, according to the average rate $\alpha = (1.48 \pm 0.12) \times 10^{-11}$ Gy^{-1}. These results represent an important step toward the full development of the X-ray nanopatterning technique.

1. INTRODUCTION

In the field of electronics based on complementary metal oxide semiconductor (CMOS) technology, during the past few decades the efforts to keep the pace of Moore's law have implied a general trend toward miniaturization of the transistor components in order to achieve lower power consumption and higher integration density. However, it is apparent that when approaching the length scale of solid-state interatomic distances many issues are expected to arise. For instance, larger impedances and fluctuations can be predicted, and this is the reason why the 10 nm technological node has seen the gradual use of germanium and III−V compounds instead of pure silicon for the transistor channels, because of their higher mobility.[1]

On the other hand, from the point of view of the patterning techniques, this trend has naturally pointed toward the use of shorter and shorter radiation wavelengths λ for the photolithographic processes in order to achieve higher and higher resolutions R, according to the Rayleigh criterion $R = k\lambda/NA$. Unfortunately, this route has encountered major problems concerning the power of the radiation sources, the requirements for mask contrast and alignment, and about the resist resolution. As an example, in the case of $\lambda \lesssim 10$ nm (i.e., in the soft X-ray regime), a proximity X-ray lithography technique very similar to ordinary optical photolithography has been tested,[2] but the need for very tight control over the mask−substrate separation, mask deformation problems, and sensitivity to vibrations during the masking process have prevented it from being adopted for mass production. Another example is represented by the electron beam lithography (EBL), which routinely achieves very good resolutions due to

Received: January 17, 2021
Revised: May 7, 2021
Published: May 18, 2021

the extremely short de Broglie wavelength, but so far it has not been able to overcome the limits of slow speeds and ineffectiveness for three-dimensional (3D) fabrication. Therefore, nowadays complicated multiple patterning photolithographic processes exploiting the λ = 193 nm radiation of ArF lasers still represent the reference technology for the mass production of 10 nm chips.

However, in all of the above-mentioned examples the use of some photoresists is implied, and an additional pattern transfer step is needed after exposure and development to complete the nanofabrication process via subsequent etching or deposition. Actually, in recent times, the increasing availability of intense radiation sources with nanometric spot size, in principle, has made it possible to imagine another photoresist-free nanofabrication approach based on the direct interaction between the chip material and the radiation, because the corresponding very high energy density is able to directly modify the material properties. Indeed, it has been observed many times that synchrotron radiation is able to trigger phenomena such as photoreduction,[3] photodissociation,[4] phase transition[5] or crystallization,[6,7] which can radically change structure and properties of the irradiated materials. In this respect, the entry into service of the fourth-generation synchrotron radiation sources[8] is expected to push the energy density at even higher limits where new states of matter should become accessible, making these phenomena more and more important and opening new possibilities for their exploitation.

In the past, our group has also observed some modifications in high-T_c superconducting oxides like $Bi_2Sr_2CaCu_2O_{8+\delta}$ (Bi-2212) and $YBa_2Cu_3O_{7-x}$ (YBCO), where we showed that irradiation with X-ray nanobeams is able to change the length of the *c*-axis lattice parameter, the electrical resistivity, and the critical temperature T_c.[9−14] Following this general idea, we have successfully exploited these changes to pattern some superconducting devices via a direct-write X-ray nanopatterning technique.[15,16] That was an important development because, in principle, this method could offer interesting advantages in terms of simplicity, real-time monitoring during device fabrication, better heat dissipation, and absence of chemical contaminations.

Even though we have already extended this approach also to a semiconducting material like TiO_2,[17] nevertheless the microscopic mechanisms responsible for the material modifications are not known yet. Among the ones that we have already investigated, it has become increasingly clear that both the oxygen knock-on and the local heating induced by the photoelectron cascades can only play quite a limited role.[18,19]

A better knowledge of these mechanisms and how they affect the material micro- and nanostructure is absolutely needed for the improvement of this X-ray nanopatterning method.

Therefore, the goal of the present paper is represented by increasing the knowledge about the structural changes induced at the micron and submicron scale by X-ray irradiation in a superconducting oxide and how these changes correlate with the corresponding modifications in the normal state and superconducting electrical properties.

2. EXPERIMENTAL SETUP AND PROCEDURES

Bi-2212 whiskers were grown according to the glassy precursor route.[20,21] High-purity commercial oxides Bi_2O_3, $SrCO_3$, $CaCO_3$, and CuO were thoroughly mixed in a Bi:Sr:Ca:Cu ratio of 1.5:1:1:2 and then put into a crucible and melted at 1150 °C in air for 30 min. Glassy plates were produced by quenching the melt between two copper plates at room temperature, and then the crystal growth took place by annealing these plates at 850 °C for 120 h in a constant oxygen flow via a growth mechanism involving shape and size changing, moving, and multiple growth interfaces.[22,23]

This process produces microscopic parallelepiped crystals of Bi-2212 with an orthorhombic structure and facets (001), (010), and (100). The typical lengths of these microcrystals are very anisotropic (about 500 μm along the *a*-axis, 10 μm along the *b*-axis and about 1 μm along the *c*-axis), and consequently, they can be oriented simply by inspection.

Very straight and defect-free crystals were selected at the optical microscope (100 × magnification) for device fabrication and mechanically transferred onto glassy substrates, which were chosen to avoid spurious contributions of the diffraction pattern. The *c*-axis of the crystals was always oriented normal to the substrate. Four Ag electrical contacts (2.1 μm in thickness) were deposited on each crystal by means of physical vapor deposition through a metallic shadow mask. In order to secure good electrical contact with the crystals without changing their oxygen stoichiometry, samples underwent an annealing procedure at 450 °C in pure oxygen atmosphere, with a heating and cooling rate equal to 5 K min^{-1}.[24] At least two Pt markers (pillars) about 1 × 1 × 1 μm^3 in size were fabricated in each sample, close to the region of interest, in order to introduce reference points to facilitate the alignment during the synchrotron experiments. These markers were deposited via focused-ion-beam (FIB)-assisted vapor deposition with a FEI Quanta 3D system, using a Ga-ion current of about 10 pA. In Figure 1, panels a and b show a scanning electron microscope (SEM) image and a geometrical sketch of the typical sample region located between the voltage contacts, respectively.

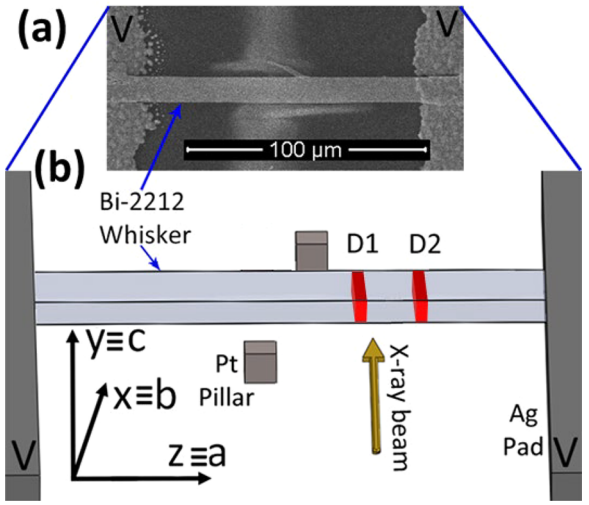

Figure 1. (a) SEM image of a typical Bi-2212 microcrystal mounted on a chip for XRD, X-ray irradiation, and four-probe electrical measurements (only the portion of the crystal between the two voltage electrodes V is shown). (b) Schematic representation of a sample with two damaged positions (D1 and D2) highlighted in the Bi-2212 crystal. Two Pt markers (pillars) are also indicated (not visible in panel (a)). The reference system shows the relative orientation of the laboratory frame of reference (*x*, *y*, and *z*) and of the Bi-2212 crystal axes (*a*, *b* ,and *c*).

Both XRD acquisition and X-ray irradiation sessions were carried out at the ID13 beamline of the European Synchrotron Radiation Facility (ESRF) in Grenoble, France. This is a long-canted beamline with the experimental hutch (EH3) placed about 100 m downstream of the undulator. The experiment was carried out at the energy E = 14.85 keV with a time-averaged photon flux $\Phi_0 = 7.53 \times 10^8$ ph s^{-1} in the 7/8 + 1 filling mode for the storage ring. The sizes of the beam

https://doi.org/10.1021/acs.cgd.1c00055
Cryst. Growth Des. 2021, 21, 3299−3309

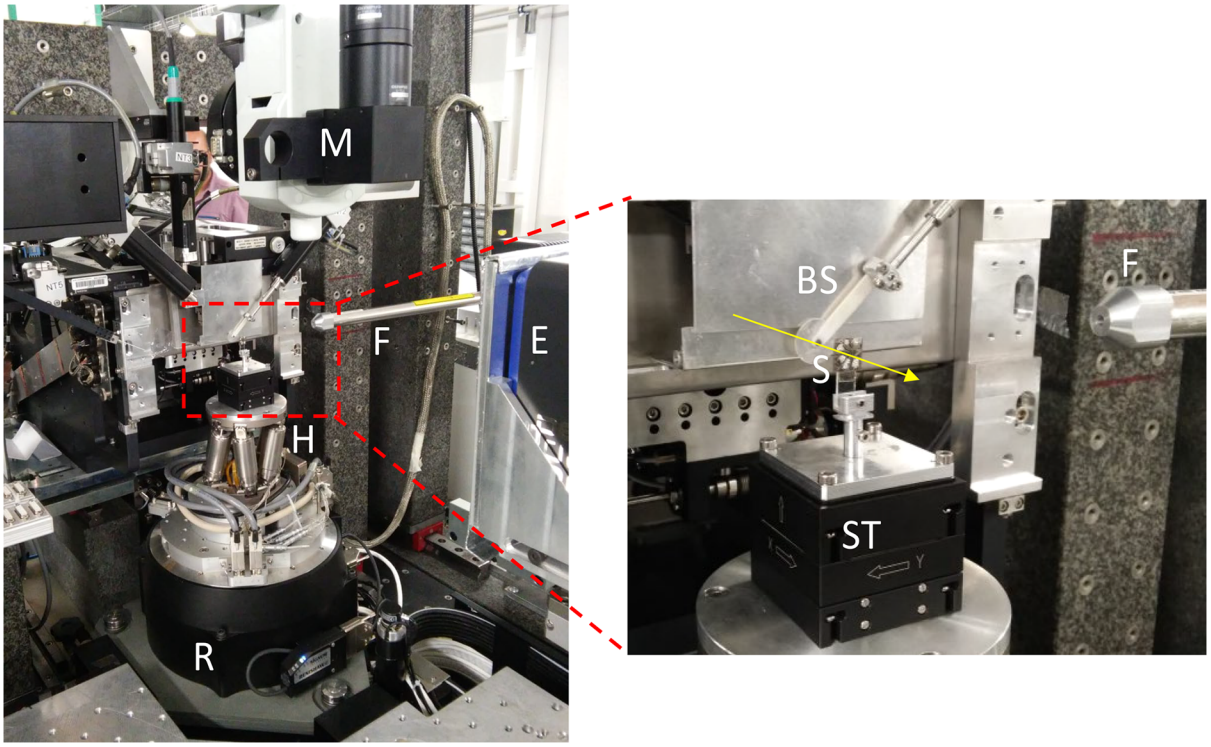

Figure 2. End-station of the experimental setup in the experimental hutch EH3 of the beamline ID13 at ESRF. The yellow line represents the X-ray nanobeam. S indicates the sample, BS is the beam stopper, ST is the sample stage, F is the fluorescence detector, M is the alignment optical microscope, H indicates the hexapod, R is the rotation stage, and E is the Eiger X 4M detector.

spot used for our experiments were 250 × 250 nm^2, and details about the monochromator and the focusing optics are reported in ref 25. Motorized positioners for the samples form a stack consisting, from bottom to top, of a rotational stage (ϕ-coordinate) with its rotation axis perpendicular to the storage ring, a hexapod, and a three-dimensional translation (x,y,z-coordinates) piezoelectric stage for high-resolution sample scanning (see Figure 2). Samples were mounted on the piezo-stage and placed with their crystallographic a-axis coinciding with the rotation axis of the setup. A microscope with the optical axis coinciding with the beam and a fluorescence detector were used for sample location and prealignment.

XRD data were acquired by means of an EIGER X 4M hybrid pixel detector from DECTRIS with 75 × 75 μm^2 pixel size and 3 μs dead time. The detector was placed at about 360 mm from the sample and horizontally translated in order to improve angular resolution and to avoid the impingement of the direct beam (see Figure S1 of the Supporting Information). Precise position and distance with respect to the beam and to the sample were evaluated by using the average of 100 diffraction patterns obtained from different positions of a boron glass capillary 0.1 mm in diameter and filled with standard corundum powder (NIST 676a), and from the refinement algorithm implemented in the FIT2D code.[26] Typical XRD characterization procedures are represented by y,ϕ-scanning and y,z,ϕ-scanning, which were used to determine sample fine orientation and twist, and y,z-scanning at fixed rotation angle ϕ, which was exploited to localize the different crystal domains. In order not to induce unwanted damage in the samples, during characterization measurements the exposure time was kept as short as 20−50 ms per point.

Off-line electrical characterization of the samples was carried out by using the four electrical probes deposited on every chip, measuring the voltage drop along the crystallographic a-axis. The electrical resistance R was measured as a function of the temperature T in a continuous He flow Janis ST-100 cryostat in the temperature range 40−295 K during temperature ramps performed on warming at a constant rate (0.7 K min^{-1}). Samples were fed with a constant current in the range 1−20 μA (depending on sample conditions), and the voltage drop was monitored by a Keithley 182 digital voltmeter.

The experimental protocol consisted of (i) R vs T characterization of each sample before X-ray irradiation; (ii) XRD characterization of the sample in pristine conditions; (iii) prolonged X-ray irradiation of a selected region of the sample; (iv) repetition of the XRD characterization for the irradiated region and its surroundings; (v) repetition of R vs T characterization after sample irradiation. Stages from (ii) to (v) were expected to be repeated at least for another unirradiated portion of the same sample. However, because of constraints related to the available beamtime, this repetition has been possible for a single sample (WBLS24), whereas another sample (WBLS03) went only through step (i) to (v). Other samples were not able to go beyond stage (iv) and therefore will be excluded from the present paper.

The most interesting samples were also characterized after the irradiation process through atomic force microscopy (AFM) in a Cypher S system by Asylum Research available at the Partnership for Soft Condensed Matter (PSCM) of ESRF.

3. DATA TREATMENTS, RESULTS AND DISCUSSION

Bi-2212 features a complex, incommensurably modulated, layered structure with superspace group *Bbmb* (0β1) and a pseudo-tetragonal cell ($a \approx b \approx 5.4$ Å, $c \approx 30.7$ Å) with modulation vector $q^* = (0, 0.210, 1)$.[27] The overstoichiometric oxygen content δ, due to oxygen atoms hosted in an interstitial site between the BiO and SrO layers,[27] strongly affects the transport properties by doping the system with holes. For instance, an increase of δ induces a decrease of the normal-state electrical resistivity and also affects its critical temperature T_c. The highest T_c (optimal doping regime, OP) corresponds only to a specific δ value, whereas both higher and lower values induce lower T_c's (overdoped regime, OD, and underdoped regime, UD, respectively).

In the present paper, all of the XRD scanning acquisitions were subjected to image treatment procedures via a Python code developed *ad hoc* (based on NumPy and Matplotlib

https://doi.org/10.1021/acs.cgd.1c00055
Cryst. Growth Des. 2021, 21, 3299−3309

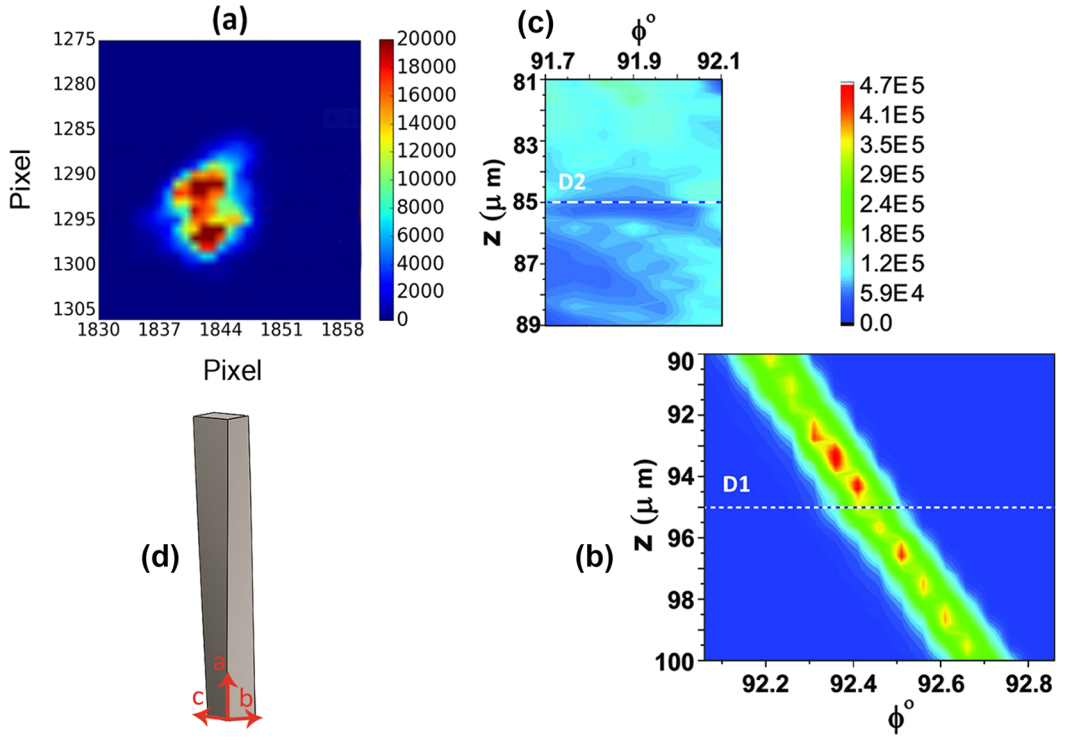

Figure 3. (a) Maximum intensity projection of the *y*,*z*,*ϕ*-scanning for the peak (006 1) measured in *pristine conditions*. (b) Corresponding localization map, integrated over the *y* coordinate. Damage position D1 is indicated and corresponds to $z = 95$ μm. (c) Localization map for the same peak obtained with the same integration technique around damage position D2 *after the irradiation*. The damage position is indicated and corresponds to $z = 85$ μm. (d) Geometrical sketch of the crystal twisted along the *a*-axis as resulting from the measurement in pristine conditions (not to scale).

libraries). Indeed, the use of a two-dimensional (2D) detector jointly with *n*-dimensional scanning ($n = 2$, 3 for *y*,*z*- or *y*,*z*,*ϕ*-scanning, respectively) produces a set of 2 + *n*-dimensional data matrixes that is very difficult to be represented on two-dimensional supports. Two main procedures were applied to simplify the analysis: the former consists of performing a pixel-wise maximum projection along one or more axes of the matrix by selecting for each pixel of the detector the maximum intensity recorded over the whole data set originated during the scanning, generating a so-called *maximum intensity projection* image. The latter consists of integrating the recorded intensity over a selected area of the detector for every single image acquired during the scanning, and in plotting this integrated intensity as a function of the acquisition coordinates in order to obtain a *localization map* of the diffracted intensity.

The samples were prealigned at the optical microscope with the whisker *a*-axis perpendicular to the electric polarization of the beam and the *b*-axis parallel to the beam. Subsequently, this prealignment was slightly refined by using the Pt pillars deposited on the substrate. Indeed, their positions represent a reference point close to the region of interest, and their small displacement along the *a*-axis of the whisker in the fluorescence maps allows alignment of the surface of the substrate parallel to the direction of the beam. The full alignment was carried out directly by means of the Bi-2212 diffraction patterns following a procedure based on a series of *φ*-scans and peak integrations. The first step consists of centering the beam on the crystal via fluorescence map acquisitions and performing a *φ*-scan of about 10−20° in steps of 0.2°. This relatively small angular range keeps the sample always illuminated by the beam, although it is not perfectly aligned to the center of rotation, and at the same time allows the reflection condition to be satisfied for several (00*l* *n*) reflections. The series of images obtained by this initial *φ*-scan was maximum projected along the rotation coordinate obtaining the typical picture shown in Figure S2 of the Supporting Information. This figure allows indexing of the reflections using the *d*-spacing and localizing the detector region of interest (ROI) where the peak of interest (POI) to be selected for whisker monitoring falls. After the detector ROI was defined, a preliminary *φ* angle at which the POI was in diffraction condition was determined by using a 1D *localization map* along the *φ* coordinate only (i.e., actually, a *localization curve* or rocking curve; see Figure S4). Successively, more precise *φ* values for the POI have been obtained via finer *φ*-scans just around the preliminary position found.

As a reference case, we discuss in detail the XRD results concerning the sample with the most complete data set (WBLS24).

The pristine state of the sample was characterized by a *y*,*z*,*ϕ*-scanning with a spatial sampling resolution of 200 nm for both the *y* and *z* coordinates, and 0.05° for the *ϕ* coordinate. Figure 3a shows the maximum intensity projection of reflection (006 1), which was selected as the POI for data analysis. In order to determine the possible crystal twist induced by the sample preparation procedures, we calculated the localization map of the peak intensity integrated over the detector area reported in Figure 3a, with the additional step of summing up all the integrated intensities obtained at any fixed (z, ϕ) coordinate pair but corresponding to different *y* values. In other words, to increase the statistics, we integrated along the short direction of the crystal $c \cong y$, whose length is about 650 nm, as

https://doi.org/10.1021/acs.cgd.1c00055
Cryst. Growth Des. 2021, 21, 3299−3309

determined from SEM observation, which corresponds just to about three data sampling in this direction. The corresponding (double-integrated) localization map is reported in Figure 3b. It can be noticed that the optimal φ angle for this reflection changes linearly along the $z \cong a$-axis of the whisker, suggesting a constant twist with a value of 0.038° μm^{-1}, corresponding to the crystal habitus schematically represented in Figure 3d. This deformation could have been originated from the operations related to the mechanical mounting of the crystal on the measurement chip and to the fabrication of electrical contacts.

The c-axis lattice parameter was also determined by averaging the values calculated from the d-spacing of the reflections (006 0), (008 0), (0010 0), (0012 0), (0014 0), and (0016 0). Each d-spacing was obtained evaluating the centroid position on the curves resulting from the radial integration of a maximum projection of a 10−20° φ scan with a fine step. The value obtained for the crystal in this pristine condition is c = 30.536(5) Å, which corresponds to a heavily OD regime.[28,29]

The crystal position selected for the first damage process (labeled as D1) is located in the center of the explored region. A rocking curve of reflection (006 1) was measured with an angular resolution of 0.01° at this position revealing a FWHM ≅ 0.06°, which indicates a very good crystallinity of this sample that is comparable to the free-standing Bi-2212 crystals analyzed by our group in a previous experiment.[29]

In order to complete the characterization of the region prior to damaging, a y,z-scanning was acquired around the position D1 at the ϕ value coinciding with the maximum of the rocking curve. Figure 4a shows the maximum intensity projection of this measurement for the same portion of the detector as in Figure 3a. Since a close inspection reveals a peak structure consisting of two subpeaks, we split the peak area into two regions A1 and A2 corresponding to each subpeak, as shown in Figure 4a. The corresponding localization maps are reported in Figure 4b. It is possible to observe that both subpeaks have originated from the same region centered around position D1 (z = 95 μm). This was somehow expected from the fact that the crystal is twisted and the y,z-scanning was performed at a fixed ϕ value corresponding to the maximum of the rocking curve at position D1 only; nevertheless, the spatial coincidence of the two subpeaks testifies that it is not really possible to describe this situation in terms of different crystal domains.

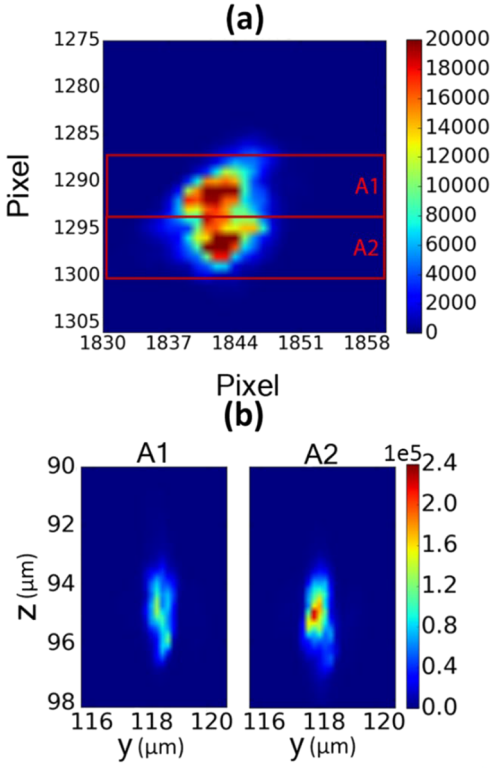

Figure 4. (a) Maximum intensity projection of the peak (006 1) (the same peak as in Figure 3a) at position D1 before irradiation. The definition of the two subpeak regions A1 and A2 is indicated by the red boxes. (b) Localization maps in real space of the diffraction intensities corresponding to the subpeaks A1 and A2.

The crystal damage was performed following a single-line pattern along the y direction, with a step size Δy = 200 nm between adjacent irradiation points. Therefore, the irradiated region corresponds to a cross-section of the crystal lying in the crystallographic bc-plane. Each point has been irradiated for a time Δt, as specified in Table 1. In order to explore several orders of magnitude, the irradiation at position D1 was split into three steps (Δt = 10, 100, and 1000 s for steps D1.a, D1.b, and D1.c, respectively), with intermediate y,z-scans for damage characterization.

No significant changes were detected after D1.a and D1.b irradiation steps in comparison with the pristine conditions. On the contrary, after irradiation D1.c the maximum projection of reflection (006 1) strongly elongates, and at least four different subpeaks can be defined in different areas of the detector (see Figure 5a). The corresponding localization maps are shown in Figure 5b: it is possible to observe that with moving from the subpeak B1 to the subpeak B4, the maximum of the diffracted intensity progressively shifts from lower z-values toward the irradiation position (z = 95 μm). This behavior indicates a supplementary twist of the habitus of the crystal as featured in Figure 5c: with increasing the cumulative fluence CF (or the cumulative dose CD), its shape tends to bend around the crystallographic b-axis, i.e., around the X-ray beam direction.

The same sample underwent a second damage procedure at another position labeled as D2 (z = 85 μm) that was located about 10 μm apart from position D1, i.e., far enough for the sample to be supposed in pristine conditions at this position. An off-line electrical characterization has taken place between the two irradiation sessions, as it will be discussed later. After centering of the sample at the maximum of the rocking curve, the preliminary characterization of the region around position D2 was performed by means of a y,z-scan. Figure 6a shows the maximum intensity projection for the same POI already studied in Figures 4 and 5: it can be noticed that its position on the detector has slightly changed because of the sample unmounting and remounting procedures necessary to perform the intermediate electrical characterization. Two subpeak regions A1 and A2 can be identified in this case, as highlighted by the red boxes in Figure 6a. The corresponding localization maps are reported in Figure 6b: it is possible to notice that the integrated intensity somehow moves toward higher values of the z-coordinate when passing from the subpeak A1 to the subpeak A2, reproducing a situation very similar to the one already observed in Figure 5b. This means that at this position D2 the crystal is already bent before irradiation, like the shape shown in Figure 5c, with an angular distance between the centroids of the two subpeaks equal to 0.34°, as calculated from the beam center. We do not have enough data to say

https://doi.org/10.1021/acs.cgd.1c00055
Cryst. Growth Des. 2021, 21, 3299−3309

Table 1. Parameters of the Irradiation Procedure Used to Damage the Crystal (See Text)[a]

irradiation position	irradiation step	time per point Δt (s)	F (10^8 J m^{-2})	CF (10^8 J m^{-2})	D (10^9 Gy)	CD (10^9 Gy)
D1	a	10	3.44	3.44	1.91	1.91
	b	100	34.4	37.8	19.1	21.0
	c	1000	344	382	191	212
D2	a	1000	344	344	191	191

[a] Δt is the irradiation time at each point. F and D represent the fluence and the dose delivered at each step, respectively. CF and CD represent the *cumulative* fluence and dose delivered after each step, respectively.

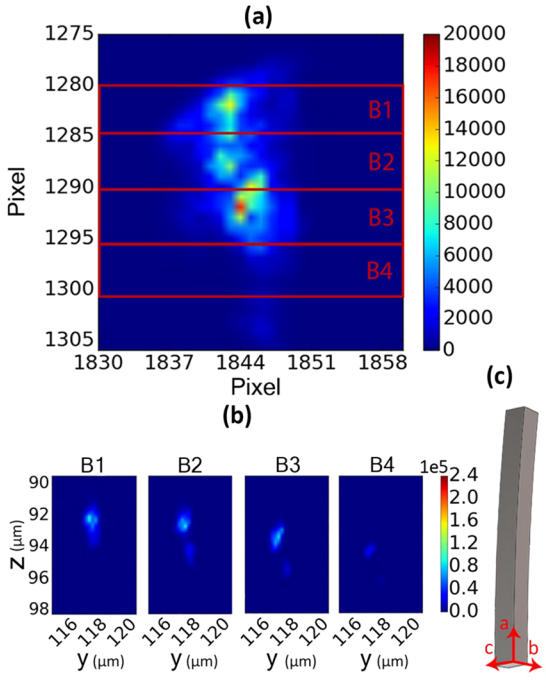

Figure 5. (a) Maximum intensity projection of reflection (006 1) after irradiation D1.c, i.e., after a cumulative dose $CD = 2.12 \times 10^{11}$ Gy and a cumulative fluence $CF = 3.82 \times 10^{10}$ J m^{-2}. The definition of the subpeaks B1, B2, B3, and B4 is highlighted by red boxes. (b) Localization maps in real space of the diffraction intensities corresponding to all of the subpeaks. (c) Geometrical sketch of the shape of the crystal indicating its bending after irradiation D1.c (not to scale).

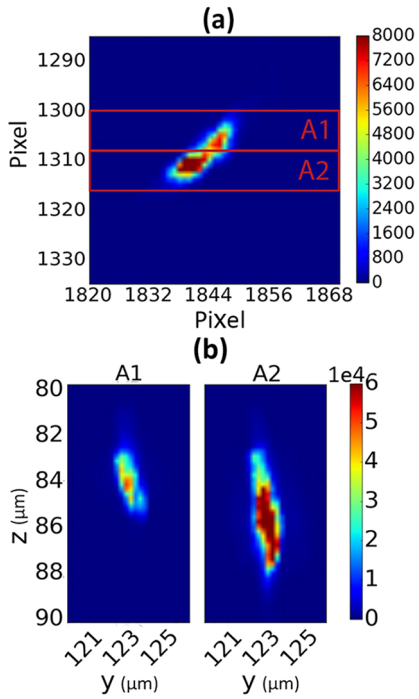

Figure 6. (a) Maximum intensity projection of reflection (006 1) measured at position D2 before irradiation. The definition of the two subpeak regions A1 and A2 is highlighted by the red boxes. (b) Localization maps in real space of the diffraction intensities corresponding to the subpeaks.

whether this curvature was already present even before the irradiation at position D1.

The irradiation procedure at position D2 has followed the same spatial pattern already used for position D1, whereas from the point of view of the time pattern only a single irradiation step D2.a was performed with Δt = 1000 s, as shown in Table 1.

The postirradiation characterization was performed via another *y*,*z*-scan whose maximum intensity projection is reported in Figure 7a. The presence of two separated subpeaks is clearly visible, with an angular distance between their centroids equal to 1.37°, as calculated from the beam center. This increase in the spread of the crystal mosaicity by about 1° is comparable to what was already observed by our group in a previous paper, even if in that case the *CF* and *CD* values were at least 20-fold larger.[29] However, this observation testifies to the appearance of two misaligned crystal domains connected by a [010]-tilted grain boundary.

The localization maps corresponding to the two subpeaks of Figure 7a are reported in Figure 7b. The results are very apparent: each subpeak is completely localized on a single side of the damaged line D2 (z = 85 μm), showing that two straight crystallites have emerged from the irradiation of the bent pristine crystal and that their grain boundary coincides with the irradiated region. This means that the irradiation has allowed releasing the local mechanical stress present in the crystal, which in turn implies a transient local change of the mechanical properties of the material occurred in the irradiated region only. The origin of this change could possibly be represented by thermal fatigue effects induced by the numerous ($\approx 6 \times 10^9$) heating/cooling cycles with ΔT = 10−30 K locally induced by the X-ray nanobeam during the irradiation time Δt, which implies corresponding thermal dilation/contraction cycles[18] or, alternatively, by transient local softening of the chemical bonds taking place during the irradiation pulses and inducing nonthermal melting in the system.[30]

As a final XRD characterization step, a *y*,*z*,ϕ-scan was performed around the position D2 after the irradiation. Following the same procedure already used for Figure 3b, a double-integrated localization map was obtained and is reported in Figure 3c. Although the data set has been somehow limited because of time constraints, some observations can be made. First, the mosaicity spread in this region

https://doi.org/10.1021/acs.cgd.1c00055
Cryst. Growth Des. 2021, 21, 3299−3309

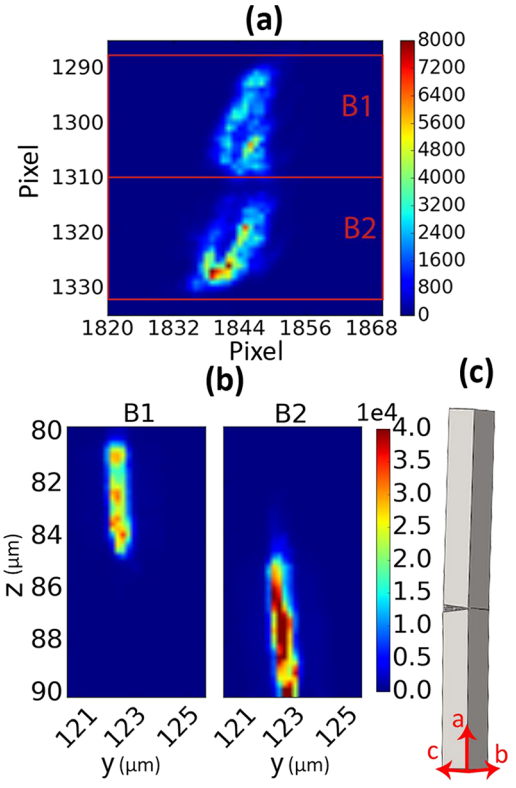

Figure 7. (a) Maximum intensity projection of reflection (006 1) measured at position D2 after irradiation with a cumulative dose $CD = 1.91 \times 10^{11}$ Gy and a cumulative fluence $CF = 3.44 \times 10^{10}$ J m^{-2}. The definition of the subpeaks B1 and B2 is highlighted by the red boxes. (b) Localization maps of the diffraction intensities corresponding to the two subpeaks. (c) Geometrical sketch of the shape of the crystal after irradiation indicating its division at position D2 ($z = 85$ μm) into two straight domains (not to scale).

after the irradiation is much greater than the one observed around position D1 in pristine conditions, with a corresponding FWHM of the rocking curve at fixed z-coordinate that can be estimated as about 0.6°, i.e., one order of magnitude larger. This fact implies that the irradiation also induces the formation of nanodomains in the crystal corresponding to [100]-tilted grain boundaries. Again, this is the same phenomenon already observed by our group in a previous paper for CD and CF values about 20-fold larger, which generated a mosaicity spread equal to about 4°.[29] However, in the present experiment, the mosaicity increase takes place at a higher rate as a function of irradiation. Indeed, a linear extrapolation of the results of the present experiment to the experimental conditions of ref 29 would result in a mosaicity of about 12°, which corresponds to a factor of 3 overestimation with respect to the experimental findings. Therefore, the comparison between these two experiments suggests that the relationship between the angular spread of the mosaicity and CD (or CF) should be nonlinear, with a lower mosaicity increase induced by higher CD and CF values. As a second observation, it can be noticed that Figure 3c shows some loss of diffracted intensity exactly at the irradiation position D2, which could be interpreted as a crystallinity loss occurring at the points where the direct interaction between the X-ray beam and the material takes place. This fact represents an indication of a rearrangement of the atomic positions according to a more disordered pattern after irradiation, whose origins could be the above-mentioned thermal fatigue or nonthermal melting.

Finally, it should be noted that the value of the c-axis lattice parameter obtained from this postirradiation scan is $c = 30.69(1)$ Å, which testifies an UD regime for the crystal that, in spite of the 20-fold lower irradiation dose, is even deeper than the one obtained in our previous experiment.[28,29]

3.1. Electrical Measurements. Complementary to the structural measurements, also electrical measurements were performed to characterize the changes in the functional properties of the crystals. For simplicity, only the measurements corresponding to another sample (WBLS03) will be discussed, whereas the ones corresponding to the sample that has been thoroughly discussed from the point of view of XRD measurements (WBLS24) can be found in the Supporting Information. This sample has undergone a single damage procedure consisting of an irradiation according a two-line raster scan with $\Delta y = 250$ nm and $\Delta z = 250$ nm, so that a square mesh was obtained for the impinging points of the beam on the crystal, with an irradiation time per point $\Delta t = 500$ s. Because of this geometrical arrangement, the irradiated portion of the crystal can be considered as a single block of homogeneous material with modified electrical properties that is electrically equivalent to a resistor placed in series with another one representing the nonirradiated regions of the crystal with their pristine electrical properties. Analogous electrical models have already been formulated in the past to interpret the photoconductivity effects and the phase instability of Bi-2212 microcrystals.[31,32]

Figure 8 shows the electrical resistance R versus temperature T behavior measured for the sample before and after the irradiation. It is clear that the irradiation has increased the total resistance of the sample, which means that the resistivity of the irradiated part ρ_{irr} is greater than the one of the pristine material ρ. A close inspection of the superconducting transition (see inset of Figure 8) reveals that the zero-resistance critical temperature $T_{c,0}$ has decreased from 71.61 K down to 70.05 K after irradiation, whereas the mean-field critical temperature T_c (defined as corresponding to the peak of the first order derivative) decreased from 76.72 to 76.08 K. The overall result of these shifts is the appearance of a longer tail for the

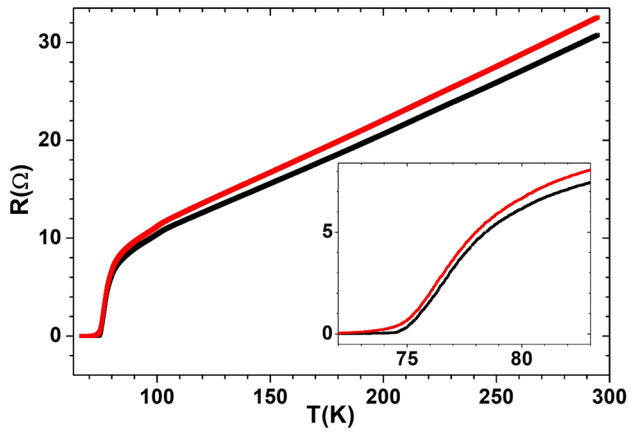

Figure 8. Resistance R vs temperature T behavior of a representative sample (WBLS03). The black line represents the sample in pristine conditions, and the red one refers to the sample after irradiation with cumulative dose $CD = 1.01 \times 10^{11}$ Gy and cumulative fluence $CF = 1.72 \times 10^{10}$ J m^{-2}. The inset zooms in the transition region.

https://doi.org/10.1021/acs.cgd.1c00055
Cryst. Growth Des. 2021, 21, 3299−3309

superconducting transition, which has already been ascribed in the past to the generation of spatially separated nanodomains with lower local values for T_c and higher values of resistivity in comparison with the pristine material.[16,29] These changes in T_c and in resistivity are related to a local decrease in the oxygen nonstoichiometric content δ induced by the beam.[29]

Because of the in-series electrical configuration of the pristine and irradiated portions of the crystal, it is possible to determine the electrical resistivity specific to each irradiation state of the material by implementing simple geometrical considerations. Indeed, for the pristine sample $R = \rho\frac{l}{S}$, where ρ is the resistivity of the material in pristine conditions, S is the cross-section area of the sample, and l is the length of the crystal as sensed by the four-probe configuration. On the other hand, after the irradiation, the total resistance of the sample R_{irr} can be described as $R_{irr} = \rho\frac{l - l_{irr}}{S} + \rho_{irr}\frac{l_{irr}}{S}$, where ρ_{irr} is the resistivity of the irradiated material and l_{irr} is the length of the irradiated portion of the crystal. Since ρ can be determined from the preliminary R vs T and geometrical characterizations, ρ_{irr} can be obtained from the following equation:

$$\rho_{irr} = R_{irr}\frac{S}{l_{irr}} - \rho\frac{l - l_{irr}}{l_{irr}} \quad (1)$$

provided that the length of the irradiated region l_{irr} is known.

Figure 9 shows the comparison between the ρ vs T behaviors of both the pristine materials and the irradiated

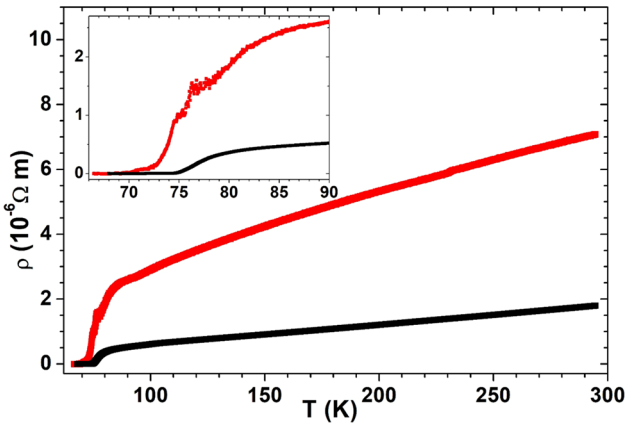

Figure 9. Resistivity vs temperature behavior of the material corresponding to the sample shown in Figure 8. The black line represents the resistivity ρ in pristine conditions, the red line represents the resistivity ρ_{irr} after the irradiation with cumulative dose $CD = 1.01 \times 10^{11}$ Gy, and cumulative fluence $CF = 1.72 \times 10^{10}$ J m^{-2}. The inset zooms in the transition region.

material as deduced from eq 1. The curve of the pristine material corresponds to the typical OD behavior, with its linear behavior in the higher temperature region ($T > 150$ K) and a room-temperature resistivity value of about 2×10^{-6} Ω m. This is in agreement with the previous observation stemming from the value of the c-axis about the general OD nature of pristine crystals. On the other hand, the curve corresponding to the resistivity ρ_{irr} after irradiation with cumulative dose $CD = 1.01 \times 10^{11}$ Gy (and cumulative fluence $CF = 1.72 \times 10^{10}$ J m^{-2}) shows the typical features of the UD regime with the downward curvature for $T > 150$ K and a room-temperature resistivity of about 6×10^{-6} Ω m.[33] This finding confirms what we have already observed from the point of view of the elongation of the crystallographic c-axis about the ability of X-ray nanobeams to induce a decrease of the oxygen non-stoichiometric content δ[9,29] and complements this fact by establishing a quantitative relationship between the CD (or the CF) and the material resistivity. About the precision and the application limits of the method used for the resistivity data analysis, they can be deduced by means of a close inspection of the ρ_{irr} vs T curve in the region around T_c. As it can be noticed in the inset of Figure 9, a noisy behavior can be detected for the data points in the temperature range 74 K < T < 80 K, which clearly corresponds to an experimental artifact. The reason can be easily understood by considering that in the transition region, for a fixed T value, small changes of the T_c's induce dramatic changes in the values of the resistivity curves, therefore resulting in a subtraction between nonequivalent sample resistivity regimes and thus generating the artifact. These considerations imply that this method can be safely applied only far enough from both T_c values involved in the analysis (i.e., before and after irradiation), which can be determined on a case-by-case basis only.

However, the value of the material resistivity at room temperature (T = 295 K) certainly falls within the reliability range of the analysis for all of the curves, due to its very large distance in temperature from the transition regions. The corresponding values are plotted in Figure 10 as a function of

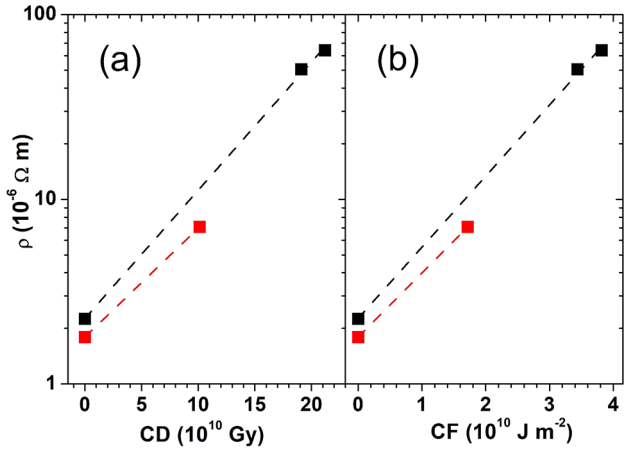

Figure 10. Resistivity of the Bi-2212 material at room temperature (T = 295 K) as a function of the cumulative dose CD (a) and of the cumulative fluence CF (b). Red and black colors refer to two different samples (WBLS03 and WBLS24, respectively). Dashed lines represent the fit to an exponential law for each sample (see text).

the cumulative dose CD and of the cumulative fluence CF for all of the samples that have completed at least one cycle of the experimental steps from (i) to (v) listed in section 2. It is possible to observe that both samples follow the exponential law $\rho = \rho_0 e^{\alpha x}$, where ρ_0 represents the material resistivity in pristine conditions, x can be identified as either CD or CF, and α is the increase rate of the resistivity with irradiation. If CD is chosen as the independent variable (see Figure 10a), then the average increase rate $\alpha = (1.48 \pm 0.12) \times 10^{-11}$ Gy^{-1} can be determined from both samples. On the other hand, if CF is selected as the independent variable (see Figure 10b), then $\alpha = (8.4 \pm 0.4) \times 10^{-11}$ J^{-1} m^2.

This observation of an exponential increase of the resistivity with irradiation deserves some comments. Indeed, it is well-known that a variation of the normal-state resistivity, along

https://doi.org/10.1021/acs.cgd.1c00055
Cryst. Growth Des. 2021, 21, 3299−3309

with corresponding changes in T_c and in the length of the *c*-axis, is a clear indication of a change in the doping status of high-temperature superconductors. Moreover, it is clear that the possibility of obtaining different doping levels ranging from OD to UD regimes is crucial to fully explore the physical properties of these materials and to clarify the underlying mechanisms responsible for their superconductivity. For instance, in the case of YBCO, a very reliable method has been developed to produce high-purity single crystals that have been extensively used to measure quantum oscillations both in the Hall and in the magneto-resistance.[34−36] This achievement has been possible also thanks to the availability of a well-defined procedure to produce detwinned single crystals with a homogeneous oxygen content corresponding to the UD regime.[37]

However, the situation is quite different in the case of Bi-2212. This material can be grown by means of the traveling solvent floating zone (TSFZ) technique in a highly reproducible way in the form of OD and OP single crystals, but the thermodynamic conditions necessary to obtain the UD regime are very close to the material decomposition line.[33] Indeed, crystals produced by directly applying a low oxygen partial pressure (minimum $p(O_2) = 5 \times 10^{-4}$ mbar) during the TSFZ process show a minimum $T_c \approx 76$ K but with significant segregation of secondary phases like CuO, Bi_2O_3, and $(Sr,Ca)_2CuO_3$ that indicate a partial decomposition of Bi-2212.[38] More often, UD crystals have been obtained by means of a postannealing stage with very low oxygen partial pressure (or vacuum). Typically, these procedures result in only moderately UD samples with $T_c \geq 65$ K.[28,33,39] This is the reason why the partial substitution of 3+ valence atoms for 2+ cations (e.g., Bi^{3+} for Sr^{2+}, or Y^{3+} for Ca^{2+}) has been tried several times to induce arbitrary small doping regimes.[39−43] By means of this technique, it has been possible to systematically explore the full doping range of $Bi_2Sr_2Ca_{1-y}Y_yCu_2O_8$ from OD to UD all the way down to the insulating behavior, detecting the metal−insulator transition at $y = 0.45$.[42] In this context, the minimum T_c observed has been $T_c \approx 35$ K, corresponding to $y = 0.42$ and to a room-temperature resistivity $\rho \approx 20 \times 10^{-6}$ Ω m. Similar results ($T_c \approx 50$ K and $\rho \approx 30 \times 10^{-6}$ Ω m at room temperature) have been obtained by a parallel systematic study.[41] Although we have not performed a systematic study as a function of *CD* and *CF* so far, a preliminary comparison between the Bi-2212 properties emerging from our heaviest irradiation conditions (i.e., $T_c \approx 48$ K and $\rho \approx 64 \times 10^{-6}$ Ω m, see also Figure S5 in the Supporting Information) and the ones obtained by means of cation substitution shows that the UD status induced in our case substantially preserves the same value of T_c even if the normal-state resistivity is larger by at least a factor of 2. This observation seems to suggest that, given the same level of normal-state resistivity ρ, the Bi-2212 underdoping process via irradiation preserves the superconducting properties more than cation substitution. It is also true that T_c values as low as $T_c \approx 29$ K and $T_c \approx 22$ K have been reported for low $p(O_2)$ annealing[44] or mixed cation substitution plus low $p(O_2)$ annealing[43] methods, respectively, but in these cases the absence of normal-state resistivity data and the presence of a small Meissner fraction prevent making a proper comparison with our results. On the other hand, by comparing our measurements to the ones carried out on whisker-like single crystals similar to ours,[28] it is possible to observe that the same value of *c*-axis lattice parameter ($c = 30.69(1)$ Å) in our case corresponds to a T_c value that is at least 20 K less that what can be obtained by means of ordinary annealing processes. This seems to indicate that X-ray irradiation has a much stronger effect on the UD status of single crystals compared to ordinary low-pressure annealing procedure. Therefore, our X-ray irradiation method sits between the cation substitution and the low $p(O_2)$ annealing procedures in terms of the power to modify the Bi-2212 properties. Consequently, it is worth further investigation since it could offer a unique opportunity to access highly UD superconducting regimes with peculiar features that are not available otherwise.

Finally, it should be noted that, from the point of view of the X-ray nanopatterning, the exponential dependence of the resistivity on the irradiation represents the phenomenological basis that has allowed us to produce Josephson devices[16] and that sets the framework for both limits and opportunities in terms of possible resistivity contrast to be achieved in the future developments of this method.

4. CONCLUSIONS

We have carefully characterized superconducting Bi-2212 crystals by means of an X-ray nanobeam and of scanning methods exploiting short exposure times. We have also irradiated selected portions of the crystals up to cumulative doses of the order of 10^{11}Gy and cumulative fluences of the order of 10^{10} J m^{-2} by means of long exposure times. It has turned out that these localized irradiations can bend the crystals or, if some bending is already present, can induce the stress release via the appearance of grain boundaries and spatially separated crystal domains. We have observed that irradiated regions undergo a decrease in their degree of crystallinity and feature an increase in their mosaicity spread. Thanks to the well-defined geometry of the crystals and their mounted-on-chip configuration, we have also been able to determine the resistivity versus temperature curves corresponding to any irradiation stage of the material by means of a subtraction method. This has allowed us to observe for the first time an exponential dependence of the Bi-2212 resistivity on the irradiation dose or fluence, which opens the way toward very interesting opportunities to access highly UD superconducting regimes for this material. We think that these results represent an important step toward the development and the reliability of the X-ray nanopatterning technique.

■ ASSOCIATED CONTENT

Supporting Information

The Supporting Information is available free of charge at https://pubs.acs.org/doi/10.1021/acs.cgd.1c00055.

Details about XRD experimental setup, peak indexing and localization, additional electrical measurements and data treatment for the multiple irradiation case (PDF)

■ AUTHOR INFORMATION

Corresponding Author

Marco Truccato − *Department of Physics, Interdepartmental Centre NIS, University of Torino, I-10125 Torino, Italy;* orcid.org/0000-0003-1564-221X; Email: marco.truccato@unito.it

https://doi.org/10.1021/acs.cgd.1c00055
Cryst. Growth Des. 2021, 21, 3299−3309

Authors

Muhammad Waqas Rabbani − *Department of Physics, Interdepartmental Centre NIS, University of Torino, I-10125 Torino, Italy*

Valentina Bonino − *Department of Physics, Interdepartmental Centre NIS, University of Torino, I-10125 Torino, Italy;* orcid.org/0000-0002-3616-5494

Luca Spessa − *Department of Physics, Interdepartmental Centre NIS, University of Torino, I-10125 Torino, Italy*

Angelo Agostino − *Department of Chemistry, Interdepartmental Centre NIS and INSTM Centro di Riferimento, University of Torino, I-10125 Torino, Italy*

Natascia De Leo − *Nanofacility Piemonte INRiM (Istituto Nazionale di Ricerca Metrologica), 10135 Torino, Italy;* orcid.org/0000-0003-2154-1108

Carmelo Prestipino − *ISCR (Institut des Sciences Chimiques de Rennes) - UMR 6226, F-35000 Rennes, France;* orcid.org/0000-0002-8541-7766

Complete contact information is available at: https://pubs.acs.org/10.1021/acs.cgd.1c00055

Notes

The authors declare no competing financial interest.

■ ACKNOWLEDGMENTS

We thank the ESRF for allocation of beamtime at the beamline ID13, for AFM support at the Partnership for Soft Condensed Matter (PSCM), and for the kind availability of all of its staff. We gratefully acknowledge Compagnia di San Paolo for financial support to NanoFacility Piemonte at INRIM. This work has been partly supported by the project NANO-X jointly approved and funded by University of Torino and Compagnia di San Paolo. M.W.R., V.B., L.S., and M.T. also acknowledge partial support from the "Departments of Excellence" (L. 232/2016) grant, funded by the Italian Ministry of Education, University and Research (MIUR).

■ REFERENCES

(1) Radamson, H. H.; Zhu, H. L.; Wu, Z. H.; He, X. B.; Lin, H. X.; Liu, J. B.; Xiang, J. J.; Kong, Z. Z.; Xiong, W. J.; Li, J. J.; Cui, H. S.; Gao, J. F.; Yang, H.; Du, Y.; Xu, B. Q.; Li, B.; Zhao, X. W.; Yu, J. H.; Dong, Y.; Wang, G. L. State of the Art and Future Perspectives in Advanced CMOS Technology. *Nanomaterials* **2020**, *10* (8), 1555.

(2) Vladimirsky, Y.; Bourdillon, A.; Vladimirsky, O.; Jiang, W.; Leonard, Q. Demagnification in proximity x-ray lithography and extensibility to 25 nm by optimizing Fresnel diffraction. *J. Phys. D: Appl. Phys.* **1999**, *32* (22), L114−L118.

(3) Stanley, H. B.; Banerjee, D.; van Breemen, L.; Ciston, J.; Liebscher, C. H.; Martis, V.; Merino, D. H.; Longo, A.; Pattison, P.; Peters, G. W. M.; Portale, G.; Sen, S.; Bras, W. X-ray irradiation induced reduction and nanoclustering of lead in borosilicate glass. *CrystEngComm* **2014**, *16* (39), 9331−9339.

(4) Huang, Z. F.; Bartels, M.; Xu, R.; Osterhoff, M.; Kalbfleisch, S.; Sprung, M.; Suzuki, A.; Takahashi, Y.; Blanton, T. N.; Salditt, T.; Miao, J. W. Grain rotation and lattice deformation during photo-induced chemical reactions revealed by in situ X-ray nanodiffraction. *Nat. Mater.* **2015**, *14* (7), 691−695.

(5) Adriaens, A.; Quinn, P.; Nikitenko, S.; Dowsett, M. G. Real Time Observation of X-ray-Induced Surface Modification Using Simultaneous XANES and XEOL-XANES. *Anal. Chem.* **2013**, *85* (20), 9556−9563.

(6) Feldman, Y.; Lyahovitskaya, V.; Leitus, G.; Lubomirsky, I.; Wachtel, E.; Bushuev, V. A.; Vaughan, G.; Barkay, Z.; Rosenberg, Y. X-ray initiation of nonthermal growth of single crystal pyramids in amorphous barium titanate. *Appl. Phys. Lett.* **2009**, *95* (5), 051919.

(7) Martis, V.; Nikitenko, S.; Sen, S.; Sankar, G.; van Beek, W.; Filinchuk, Y.; Snigireva, I.; Bras, W. Effects of X-rays on Crystal Nucleation in Lithium Disilicate. *Cryst. Growth Des.* **2011**, *11* (7), 2858−2865.

(8) Liuzzo, S. M.; Carmignani, N.; Franchi, A.; Perron, T.; Scheidt, K. B.; Taurel, E.; Torino, L.; White, S. M. Iop, Preparation of the EBS beam commissioning. In *10th International Particle Accelerator Conference*; Iop Publishing Ltd: Bristol, 2019; Vol. *1350*, p 012022.

(9) Pagliero, A.; Mino, L.; Borfecchia, E.; Truccato, M.; Agostino, A.; Pascale, L.; Enrico, E.; De Leo, N.; Lamberti, C.; Martinez-Criado, G. Doping Change in the Bi-2212 Superconductor Directly Induced by a Hard X-ray Nanobeam. *Nano Lett.* **2014**, *14* (3), 1583−1589.

(10) Plapcianu, C.; Agostino, A.; Badica, P.; Aldica, G. V.; Bonometti, E.; Ieluzzi, G.; Popa, S.; Truccato, M.; Cagliero, S.; Sakka, Y.; Vasylkiv, O.; Vidu, R. Microwave Synthesis of Fullerene-Doped MgB_2. *Ind. Eng. Chem. Res.* **2012**, *51* (34), 11005−11010.

(11) Mino, L.; Borfecchia, E.; Agostino, A.; Lamberti, C.; Truccato, M. Oxygen doping tuning in superconducting oxides by thermal annealing and hard X-ray irradiation. *J. Electron Spectrosc. Relat. Phenom.* **2017**, *220*, 69−75.

(12) Gozzelino, L.; Gerbaldo, R.; Ghigo, G.; Laviano, F.; Truccato, M. Comparison of the Shielding Properties of Superconducting and Superconducting/Ferromagnetic Bi- and Multi-layer Systems. *J. Supercond. Novel Magn.* **2017**, *30* (3), 749−756.

(13) Bonino, V.; Mino, L.; Agostino, A.; Prestipino, C.; Fretto, M.; Truccato, M. Tuning the functional properties of $YBa_2Cu_3O_{7-\delta}$ by synchrotron X-ray irradiation. In *Optics Damage and Materials Processing by Euv/X-Ray Radiation VII*; Juha, L.; Bajt, S.; Guizard, S., Eds.; Spie-Int Soc Optical Engineering: Bellingham, 2019; Vol. *11035*, p UNSP 110350I.

(14) Gozzelino, L.; Minetti, B.; Gerbaldo, R.; Ghigo, G.; Laviano, F.; Lopardo, G.; Plapcianu, C.; Agostino, A.; Cagliero, S.; Truccato, M.; Zilberti, L.; Mezzetti, E. Magnetic Characterization of MgB_2 Bulk Superconductor for Magnetic Field Mitigation Solutions. *J. Supercond. Novel Magn.* **2011**, *24* (1−2), 307−312.

(15) Mino, L.; Bonino, V.; Agostino, A.; Prestipino, C.; Borfecchia, E.; Lamberti, C.; Operti, L.; Fretto, M.; De Leo, N.; Truccato, M. Maskless X-Ray Writing of Electrical Devices on a Superconducting Oxide with Nanometer Resolution and Online Process Monitoring. *Sci. Rep.* **2017**, *7* (1), 9066.

(16) Truccato, M.; Agostino, A.; Borfecchia, E.; Mino, L.; Cara, E.; Pagliero, A.; Adhlakha, N.; Pascale, L.; Operti, L.; Enrico, E.; De Leo, N.; Fretto, M.; Martinez-Criado, G.; Lamberti, C. Direct-Write X-ray Nanopatterning: A Proof of Concept Josephson Device on $Bi_2Sr_2CaCu_2O_{8+\delta}$ Superconducting Oxide. *Nano Lett.* **2016**, *16* (3), 1669−1674.

(17) Mino, L.; Bonino, V.; Picollo, F.; Fretto, M.; Agostino, A.; Truccato, M. Tailoring the Local Conductivity of TiO_2 by X-Ray Nanobeam Irradiation. *Adv. Electron. Mater.* **2019**, *5* (6), 1900129.

(18) Bonino, V.; Torsello, D.; Prestipino, C.; Mino, L.; Truccato, M. Time and space resolved modelling of the heating induced by synchrotron X-ray nanobeams. *J. Synchrotron Radiat.* **2020**, *27*, 1662−1673.

(19) Torsello, D.; Mino, L.; Bonino, V.; Agostino, A.; Operti, L.; Borfecchia, E.; Vittone, E.; Lamberti, C.; Truccato, M. Monte Carlo analysis of the oxygen knock-on effects induced by synchrotron x-ray radiation in the $Bi_2Sr_2CaCu_2O_{8+\delta}$ superconductor. *Phys. Rev. Mater.* **2018**, *2* (1), 014801.

(20) Matsubara I, T. H.; Ogura, T.; Yamashita, H.; Kinoshita, M.; Kawai, T. Preparation of the Bi(Pb)-Sr-Ca-Cu-O fibrous crystals containing the high-T_c phase. *Japan. J. Appl. Phys. Lett.* **1989**, *28* (8), L1358−L1360.

(21) Latyshev, Y. I.; Gorlova, I.G.; Nikitina, A.M.; Antokhina, V.U.; Zybtsev, S.G.; Kukhta, N.P.; Timofeev, V.N. Growth and study of single-phase 2212 BSCCO whiskers of submicron cross-sectional area. *Phys. C* **1993**, *216* (3−4), 471−477.

(22) Badica, P.; Agostino, A.; Khan, M. M. R.; Cagliero, S.; Plapcianu, C.; Pastero, L.; Truccato, M.; Hayasaka, Y.; Jakob, G. Bi-2212 and Y123 highly curved single-crystal-like objects: whiskers,

bows and ring-like structures. *Supercond. Sci. Technol.* **2012**, *25* (10), 105003.
(23) Cagliero, S.; Borfecchia, E.; Mino, L.; Calore, L.; Bertolotti, F.; Martinez-Criado, G.; Operti, L.; Agostino, A.; Truccato, M.; Badica, P.; Lamberti, C. Insight into non-linearly shaped superconducting whiskers via a synchrotron nanoprobe. *Supercond. Sci. Technol.* **2012**, *25* (12), 125002.
(24) Truccato, M.; Rinaudo, G.; Manfredotti, C.; Agostino, A.; Benzi, P.; Volpe, P.; Paolini, C.; Olivero, P. Growth, contacting and ageing of superconducting Bi-2212 whiskers. *Supercond. Sci. Technol.* **2002**, *15* (9), 1304−1310.
(25) Riekel, C.; Burghammer, M.; Davies, R., Progress in micro- and nano-diffraction at the ESRF ID13 beamline. In *Iop Conf Ser-Mat Sci.*; Bras, W.; Goossens, J. G. P.; Goderis, B., Eds.; Iop Publishing Ltd: Bristol, 2010; Vol. *14*, p 012013.
(26) Hammersley, A. P.; Svensson, S. O.; Hanfland, M.; Fitch, A. N.; Hausermann, D. Two-dimensional detector software: From real detector to idealised image or two-theta scan. *High Pressure Res.* **1996**, *14* (4−6), 235−248.
(27) Petricek, V. V.; Gao, Y.; Lee, P.; Coppens, P. X-ray analysis of the incommensurate modulation in the 2:2:1:2 Bi-Sr-Ca-Cu-O superconductor including the oxygen atoms. *Phys. Rev. B: Condens. Matter Mater. Phys.* **1990**, *42* (1), 387−392.
(28) Inomata, K.; Kawae, T.; Nakajima, K.; Kim, S. J.; Yamashita, T. Junction parameter control of $Bi_2Sr_2CaCu_2O_{8+\delta}$ stacked junctions by annealing. *Appl. Phys. Lett.* **2003**, *82* (5), 769−771.
(29) Bonino, V.; Agostino, A.; Prestipino, C.; Hernandez, O.; Fretto, M.; Mino, L.; Truccato, M. Structural and functional modifications induced by X-ray nanopatterning in Bi-2212 single crystals. *CrystEngComm* **2018**, *20* (42), 6667−6676.
(30) Medvedev, N.; Milov, I. Nonthermal phase transitions in metals. *Sci. Rep.* **2020**, *10* (1), 12775.
(31) Truccato, M.; Imbraguglio, D.; Agostino, A.; Cagliero, S.; Pagliero, A.; Motzkau, H.; Rydh, A. Photoconductivity effects in mixed-phase BSCCO whiskers. *Supercond. Sci. Technol.* **2012**, *25* (10), 105010.
(32) Truccato, M.; Cagliero, S.; Agostino, A.; Panetta, M.; Rinaudo, G. Electrical study of an unusual phase transformation in a $Bi_2Sr_2Ca_2Cu_3O_{10+x}$ whisker at room temperature. *Supercond. Sci. Technol.* **2006**, *19* (10), 1003−1009.
(33) Watanabe, T.; Fujii, T.; Matsuda, A. Anisotropic resistivities of precisely oxygen controlled single-crystal $Bi_2Sr_2CaCu_2O_{8+\delta}$: Systematic study on "spin gap" effect. *Phys. Rev. Lett.* **1997**, *79* (11), 2113−2116.
(34) Liang, R. X.; Bonn, D. A.; Hardy, W. N. Growth of high quality YBCO single crystals using $BaZrO_3$ crucibles. *Phys. C* **1998**, *304* (1−2), 105−111.
(35) Doiron-Leyraud, N.; Proust, C.; LeBoeuf, D.; Levallois, J.; Bonnemaison, J. B.; Liang, R. X.; Bonn, D. A.; Hardy, W. N.; Taillefer, L. Quantum oscillations and the Fermi surface in an underdoped high-T_c superconductor. *Nature* **2007**, *447* (7144), 565−568.
(36) Ramshaw, B. J.; Sebastian, S. E.; McDonald, R. D.; Day, J.; Tan, B. S.; Zhu, Z.; Betts, J. B.; Liang, R. X.; Bonn, D. A.; Hardy, W. N.; Harrison, N. Quasiparticle mass enhancement approaching optimal doping in a high-T_c superconductor. *Science* **2015**, *348* (6232), 317−320.
(37) Liang, R. X.; Bonn, D. A.; Hardy, W. N. Preparation and X-ray characterization of highly ordered ortho-II phase $YBa_2Cu_3O_{6.50}$ single crystals. *Phys. C* **2000**, *336* (1−2), 57−62.
(38) Liang, B.; Lin, C. T. On the growth of underdoped $Bi_2Sr_2CaCu_2O_{8+\delta}$ single crystals by TSFZ method. *J. Cryst. Growth* **2002**, *237*, 756−761.
(39) De Almeida-Didry, S.; Giovannelli, F.; Monot-Laffez, I.; Sidis, Y.; Bourges, P.; Schoenstein, F.; Pruvost, S.; Pignon, B. Investigations for the growth of large underdoped $Bi_2Sr_2CaCu_2O_{8+\delta}$ single crystals. *J. Cryst. Growth* **2010**, *312* (3), 466−470.
(40) Ruan, K. Q.; Cao, Q.; Li, S. Y.; Qian, G. G.; Wang, C. Y.; Chen, X. H.; Cao, L. Z. The detailed transport property of the underdoped Bi-2212 system in the pseudogap state. *Phys. C* **2001**, *351* (4), 402−408.
(41) Ruan, K. Q.; Li, S. Y.; Chen, X. H.; Qian, G. G.; Cao, Q.; Wang, C. Y.; Cao, L. Z. The systematic study of the normal-state transport properties of Bi-2212 crystals. *J. Phys.: Condens. Matter* **1999**, *11* (18), 3743−3750.
(42) Kendziora, C.; Forro, L.; Mandrus, D.; Hartge, J.; Stephens, P.; Mihaly, L.; Reeder, R.; Moecher, D.; Rivers, M.; Sutton, S. Composition, structure, and electrical-properties of $Bi_2Sr_2Ca_{1-y}Y_yCu_2O_8$ - a single-crystal study. *Phys. Rev. B: Condens. Matter Mater. Phys.* **1992**, *45* (22), 13025−13034.
(43) Yamashita, S.; Kasai, T.; Fujii, T.; Watanabe, T.; Matsuda, A. Control of carrier concentration in Bi-2212. *Phys. C* **2010**, *470*, S170−S172.
(44) Liang, B.; Lin, C. T.; Maljuk, A.; Yan, Y. Effect of vacuum annealing on the structure and superconductivity of $Bi_2Sr_2CaCu_2O_{8+\delta}$ single crystals. *Phys. C* **2002**, *366* (4), 254−262.

https://doi.org/10.1021/acs.cgd.1c00055
Cryst. Growth Des. 2021, 21, 3299−3309